# AVO Inversion and Interpretation via Localized 3D Migrations

*Wenjie Dong and Mark Ponton, Mobil E&P Technical Center*

## Summary

In this paper, we demonstrate a new approach to 3D AVO inversion and interpretation which allows interpreters to interact with the prestack 3D data volume. Central to this methodology is a one-step 3-D migration/inversion method that estimates AVO attributes (intercept and slope) by least-square minimization of data misfit over a rectangular area of CMP bins. Given a reasonable aperture (e.g., 1st Fresnel zone) and a 3D macro velocity model, the method leads to robust attribute estimation as well as good 3D structural imaging. With its unique parallel implementation on the Cray T3E, the method produces AVO attribute profiles and slices without first rendering the 3D image volume. This provides the flexibility for interpreters to validate and refine their interpretation. We illustrate these features with examples from deep water West Africa.

## Introduction

Current 3D AVO analysis relies on 3D time migration followed by either angle stacks or curve-fitting to extract AVO attributes: intercept and slope (or gradient). Frequently, the 3D time migration step involves constant velocity migration and no appropriate weighting is applied to the seismic amplitudes. Not only can this lead to inaccurate, even unreliable AVO attributes, but also less interpretable images. Moreover, once the image volume is generated, its interpretation is limited by the quality of the existing volume. Validation tends to be restricted to checking the amplitude behavior of binned gathers. Any refinement to the imaging and AVO estimation is out of the question unless the process is seriously flawed.

These limitations warrant more physical and flexible consideration of the 3D attribute extraction and imaging process. As Figure ?? illustrates, any subsurface point can be regarded as a diffractor. All CMPs, regardless of their positions, contain its traveltime and amplitude information. In 3D geometry, CMPs (or bins) in other seismic lines also include information about the diffractor. It follows naturally that, to best estimate the lithological properties of the diffractor, the inversion aperture must include CMPs within a rectangular area centered at the diffractor's surface location. Performing this inversion for all image points results in reliable 3D imaging and property estimation. Carrying it out for selected image points renders flexible profiling through the potential image volume.

In the following sections, we set up and solve the 3D AVO inversion problem for an arbitrary image point. We then comment on its parallel implementation on the Cray T3E. We also define an all-class AVO indicator: the Fluid Line section. Using two data sets from deep water West Africa, we demonstrate the advantages of our approach by comparing results with conventional method.

## 3D AVO Inversion Methodology

According to the Born scattering theory, 3D surface reflection data from subsurface scatterers can be expressed

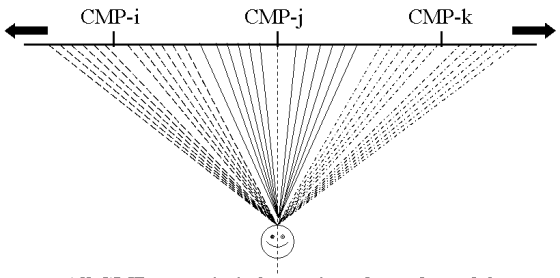


Fig. 1: Diagram showing the pertinency of all CMPs to the estimation of scatter property.

in the frequency domain as follows.

$$P_s(h, x_m, y_m, \omega) = \iiint G_a A(\underline{x}) d\underline{x} + \iiint G_b B(\underline{x}) d\underline{x}. \quad (1)$$

Here, $A$ and $B$ are the AVO intercept and slope at location $\underline{x} = (x, y, z)$. $G_a$ and $G_b$ are weighting functions dependent on the source, receiver, and scatterer locations. $P_s$ is a function of the offset ($h$), the CMP or bin location ($x_m$, $y_m$), and the angular frequency ($\omega$).

Our 3D AVO inversion algorithm proposes to determine $A(\underline{x})$ and $B(\underline{x})$ that best fit the field data approximated by equation (??). The standard least-square error minimization is used as the fit criterion. $Minimize$

$$\sum_h \iiint ||D(h, x_m, y_m, \omega) - P_s(h, x_m, y_m, \omega)||^2 d\omega dx_m dy_m, \quad (2)$$

where $D$ is the field data. The normal equations for the least square minimization with respect to $A$ and $B$ are

$$\begin{aligned} \iiint g_{aa}(\underline{x}, \underline{y}) a(\underline{x}) d\underline{x} + \iiint g_{ba}(\underline{x}, \underline{y}) b(\underline{x}) d\underline{x} &= g_{da}(\underline{y}), \\ \iiint g_{ab}(\underline{x}, \underline{y}) a(\underline{x}) d\underline{x} + \iiint g_{bb}(\underline{x}, \underline{y}) b(\underline{x}) d\underline{x} &= g_{db}(\underline{y}). \end{aligned} \quad (3)$$

Here $\underline{y} = (\xi, \eta, \zeta)$ is the ouput point and $\underline{x} = (x, y, z)$ is the actual scattering point when data were collected. Other symbols are defined as

$$\begin{aligned} g_{ij}(\underline{x}, \underline{y}) &= \textstyle\sum_h \iiint G_i(\underline{x}) G_j^*(\underline{y}) d\omega dx_m dy_m, \\ g_{dj}(\underline{y}) &= \textstyle\sum_h \iiint D(x_m, y_m, h, \omega) G_j^*(\underline{y}) d\omega dx_m dy_m, \end{aligned} \quad (4)$$

where the asterisk indicates complex conjugate. From the second definition in (??), the right hand sides of equation (??) are two migrated images. To obtain the intercept and slope at the output point, the two integral equations have to be solved.

It's impractical to solve equation (??) numerically, even under the horizontally-layered-earth assumption. Early

## 3D AVO Inversion/Interpretation

2D work in migration/inversion used the $strongly\ peaked$ assumption (Beydoun and Mendes, 1989) to approximate the Hessian matrix by its diagonal elements. Although this assumption significantly reduces computation it neglects neighboring point interaction, which is required by the least square minimization. In the 3D case, neighboring point coupling becomes more important because accurate weights are necessary for reliable attribute extraction. Moreover, to change arguments of $A$ and $B$ from $\underline{x}$ to $\underline{y}$ we need to account for the behavior of the multi-fold integrals as $\underline{y}$ approaches $\underline{x}$.

Dong and Keys (1998) proposed evaluating the Hessian asymptotically using 2D stationary phase. Synthetic and real data examples confirmed the accuracy of the method. This approach is extended to 3D to solve equation (??) as follows.

Under the assumptions of $high$ frequency data and locally 1-D velocity model (which ensures only one stationary point), a four-dimensional stationary phase approximation can be applied to the $dxdydx_mdy_m$ integrals. The stationary phase conditions require that the image point $\underline{y}$ be close to the scatterer $\underline{x}$ in order for the integrals to produce significant contribution. When $\underline{y}$ is close to $\underline{x}$, Taylor expansion of the phase leads to analytical evaluation of the $dz$ integral through the delta function generated by the $\omega$ integral.

Using the above analysis, equation (??) is reduced to the following linear algebraic equations for $A(\underline{y})$ and $B(\underline{y})$

$$W_{aa}\ A(\underline{y}) + W_{ab}\ B(\underline{y}) \ = \ M_a(\underline{y}), \qquad (5)$$

$$W_{ba}\ A(\underline{y}) + W_{bb}\ B(\underline{y}) \ = \ M_b(\underline{y}), \qquad (6)$$

where $M_a$ and $M_b$ are migrated images that emphasize the near and far offsets, respectively. And,

$$M_i = \sum_h \iint Q_i(h, x_m, y_m, \underline{y})\, D_m(h, x_m, y_m, t(\underline{y}))\, dx_m dy_m$$
$$D_m(h, x_m, y_m, t) = \int i\omega D(h, x_m, y_m, \omega) e^{-i\omega t} d\omega.$$

These equations comprise our final 3D AVO inversion algorithm. It is fundamentally different from the two-step approaches (i.e., estimating the reflection coefficients first, then AVO by curve fitting) following Bleistein (1987).

The inversion weights, $W_{ij}$, include more than just the amplitude terms of the 3D Green's function. These weights are also angle dependent. More importantly, they include curvatures of the traveltime with respect to the two horizontal coordinates of the output point. These factors together yield the amplitude correction needed for the integration of the 3-D data along the $x_m$ and $y_m$ directions.

The near and far migrations, $M_a$ and $M_b$, are quite different from the near and far angle-stacks of the time-migrated common image gathers. $M_a$ emphasizes the near offsets according to weight function $Q_a$ which spans all offsets. On the other hand, $M_b$ has more weighting on the far offsets. Through the two migrations, quality control can be performed on the background macro velocity model. Furthermore, I/O time to output two migrated images is significantly less than to output a image volume for every offset.

### Parallel Implementation on Cray T3E

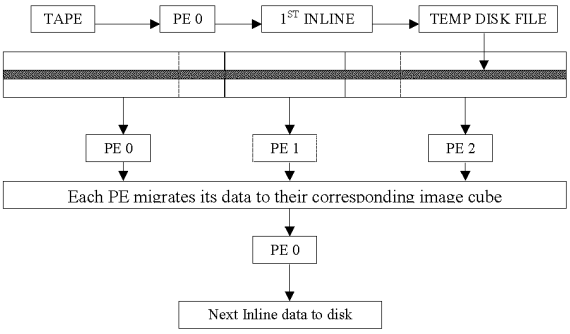


Fig. 2: T3E algorithm design and data management for the 3D AVO inversion. PE = processing element.

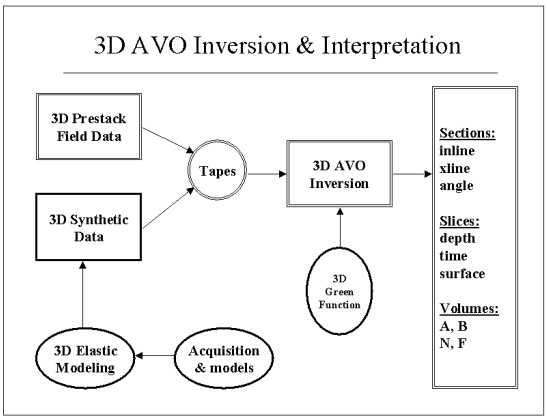


Fig. 3: Diagram showing the scope of our 3D AVO inversion and interpretation system. The lower left flow was used to generate 3D synthetic data to test the inversion algorithm. The system's flexibility allow the generation of different type of outputs for interpretation.

Given an output trace location, a rectangular area of CMPs (symmetric in both directions about the output location) are used to derive the intercept and slope. This localized implementation is desirable because stratigraphic anomalies normally are local features and can be imaged well as long as the migration aperture is one Fresnel zone wide. Limiting the migration aperture increases the algorithm efficiency and avoids contamination by noise in other part of the data. It also reduces the error caused by lateral velocity variation, thus a locally 1-D velocity model can be used.

Memory needed to hold all the CMPs within the aperture often exceeds 10 GB. This is beyond the capacity of most modern parallel computers. Therefore, memory management and adaptive algorithm design become critical. Figure ?? shows our implementation. The algorithm can be thought of as sparsely toothed comb, each tooth being the PE node. Combing along crossline direction is equivalent to migrate data in that direction. Once the PEs finish the crossline migration, they shift one CMP (bin) position along the inline direction and repeat combing in the crossline direction again.

In the implementation, users are allowed the flexibility to choose the type of output desired, as shown in Figure ??. Once the users specify output type and inversion aperture, the program will automatically determine the data range to use for the inversion.

## The Fluid Line Section

We shall use the term "Fluid Line Section" as the AVO indicator section in the following examples. A brief definition is given here. A fluid line usually refers to a shale/brine-sand background trend observable in the intercept/slope cross-plots. For a constant background $V_p/V_s$, the fluid line can be expressed as $\lambda A(\xi,\eta,t) + B(\xi,\eta,t)$. In field data situation $\lambda$ often varies with both surface location and depth, primarily due to changes in inversion aperture and the actual $V_p/V_s$. In light of this variation, we use a least square optimization with a rectangular window of the intercept/slope sections to determine a position-dependent scalar $\lambda$ and form the so-called *fluid line section*.

$$\lambda(\underline{y})A(\underline{y}) + B(\underline{y}) \quad \text{or} \quad \lambda(\xi,\eta,t)A(\xi,\eta,t) + B(\xi,\eta,t) \quad (7)$$

The fluid line section measures the normal distance of every $(A, B)$ pair to the fluid line. Thus, intercept/slope pairs that fall on the fluid line will result in zero distance (the fluid line section background). In comparison, anomalous AVO pairs will register a large distance, therefore, showing up strongly on the fluid line section. The fluid line section is an AVO indicator section that works for all AVO classes. In 3D AVO interpretation, "Fluid Line Slice" and "Fluid Line Volume" are used for prospect generation and reservoir characterization.

Due to tuning and stretching artifacts (Dong, 1999), however, the fluid line section is never as clean as one desires.

## Examples: Deep Water West Africa

As Figure ?? indicates, 3D synthetic data were generated and used for algorithm testing. Although not shown, results have validated the theoretical development. Instead, we concentrate on real data examples here.

3D seismic data from two West Africa deep water areas (Area 1 and Area 2) are analyzed using the 3D AVO inversion scheme to demonstrate its superior ability for imaging and attribute extraction. Area 1 data consist of 300 in-lines (37.5 m spacing) and 1300 cross-lines (12.5 m), which amount to a size of 200 GB. Other specifications being the same as Area 1, Area 2 has 200 inlines at a size of 140 GB. These data were flex-binned and interpolated to reduce holes in offset distribution.

### Flexibility

Figure ?? shows the Fluid Line slice of Area 1 at 3000 meters. It's one of the nine slices we instructed the program to generate. Along with several profiles these slices give some good area perspectives of the subsurface structure and AVO anomalies. It needs to be emphasized that the slicing is done without first generating the image volume.

### Comparison with 3D time migration

Figure ?? is the near angle stack (5-15 degrees) of the common image gathers after 3D time migration which was done by a large processing contractor. Special gain functions were applied to the original section so the target reflectors can show more clearly. Even with the gain functions, the time migration results are far from the quality of the 3D AVO inversion results. Figure ?? shows the intercept section of the same line generated using our outlined algorithm. No gain is applied. Note the absence of fault planes and scale imbalance in the angle stack section.

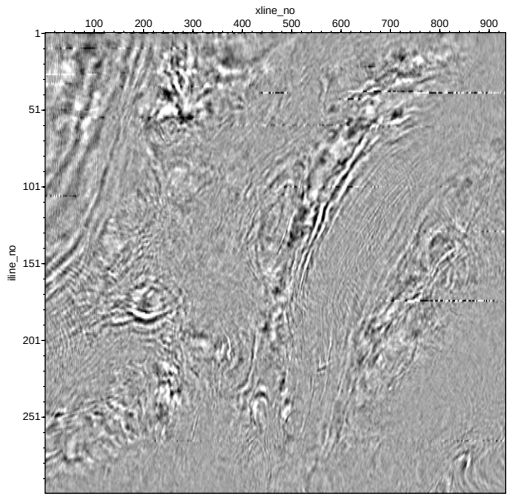


Fig. 4: Fluid Line depth slice of Area 1 at 3000 m. The slice covers about 11x11 square kilometers. It shows the extent and characteristics of the prospect near the center of the slice. Inline 101 corresponds to the profiles in Figures ?? and Figure ??.

To derive meaningful intercept and slope, the near and far angle stacks after 3D time migration often require different scaling functions prior to their combination. Due to their empirical or arbitrary nature, these gain functions are difficult to obtain and may lead to inaccurate or wrong AVO attributes. In contrast, 3D AVO inversion has rigorous specifications for the gain functions. They will lead to well-balanced and more accurate AVO attributes.

When a 3D time migration ignores relative amplitude considerations, the migration process destroys true amplitude information. AVO analysis based on these time migrated results renders inaccurate AVO attribute estimation.

### Accuracy of AVO attributes

Figure ?? is a fluid line time section in Area 2 that goes through an exploration well located at crossline 560. AVO modeling using the $P$, $S$, and density logs indicate the presence of AVO anomalies at 1.85 sec, 2.5 sec, and 2.8 sec. These events correspond to the three anomalous AVO zones shown in the Fluid Line section. This suggests the reliability of our 3D AVO inversion for attribute extraction.

To the left of the section, there is an AVO anomaly at crossline 60 and 2.3 sec. It has been designated as a prospect.

We must comment that the existence of an AVO anomaly does not necessarily mean the presence of oil or gas. Available geological and lithological information need to be carefully considered before drilling to screen out non-

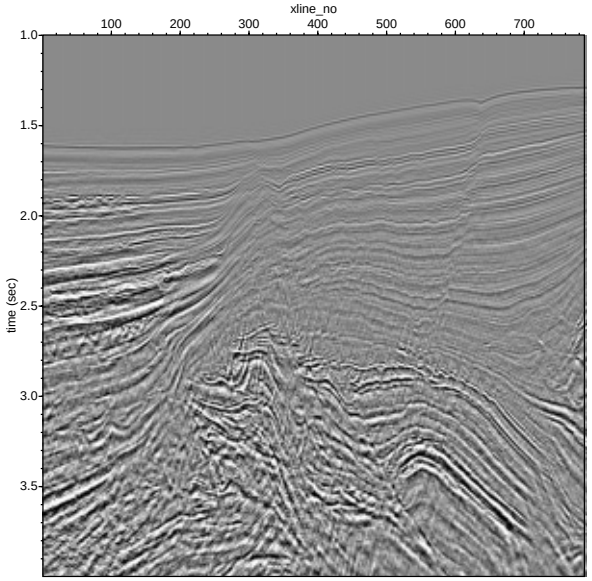


Fig. 5: Near angle stack (5-15 degrees) of the common image gathers after 3D time migration. Gain functions increasing with time are applied to boost up deeper targets so they can be more visible. Since a near angle stack can be approximately regarded as an intercept section, this section should be compared with Figure ??. This profile corresponds to inline 101 in Figure ??.

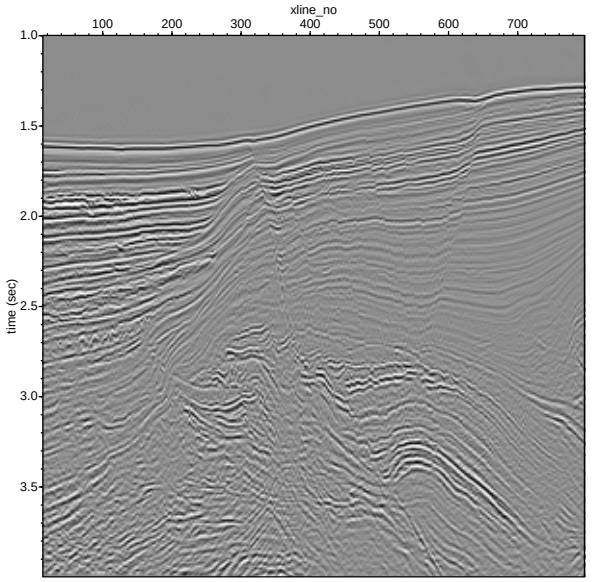


Fig. 6: The intercept (A) time section obtained by the 3D AVO inversion approach outlined in the paper. This is the same line as Figure ??. No gain is applied and the color scale is the same as the angle stack section. The depth slice of Figure ?? roughly corresponds to a time of 3.4 seconds.

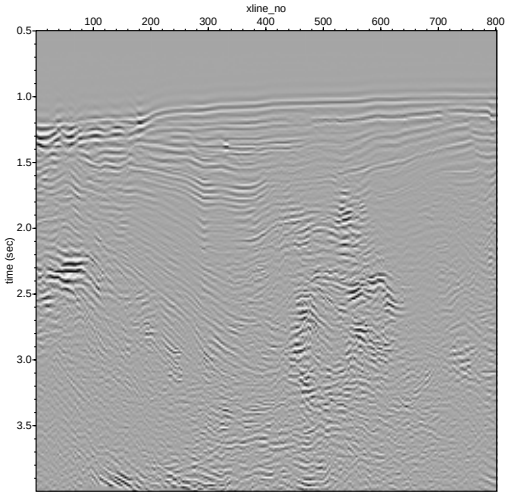


Fig. 7: Fluid Line section in time for a line in Area 2. An exploration well was drilled through the three anomalies near crossline 560. Well log analysis confirms the existence of the three AVO anomalies at 1.85, 2.5, and 2.8 seconds.

hydrocarbon and low-accumulation possibilities.

## Conclusions

We have described a new 3D AVO inversion method that estimates AVO intercept and slope through least square minimization of data misfit over a rectangular aperture. Using asymptotic analysis, we reduce the integral normal equations into an algebraic form. In doing so, reliable inversion weights are obtained through more accurate approximation of the Hessian matrix. The unique and flexible implementation on parallel computers makes interactive interpretation feasible through creating AVO indicator sections and slices. The flexibility and reliability of our 3D AVO inversion have been demonstrated by field data examples from West Africa. With 3D elastic modeling, the proposed 3D inversion and interpretation methodology should be of significant value to time-lapse 3D studies.

## Acknowledgements

We thank our colleagues J.M. Reilly and M. Mitchell for their assistance in obtaining and pre-processing of the field data, and P.S. Cunningham for careful review and comments. We also thank Mobil for the permission to publish.

## References

Beydoun, W.B., and Mendes, M., 1989, Elastic ray-Born $l_2$-migration/inversion: Geophysical J., **97**, 151-160.

Bleistein, N., 1987, On the imaging of reflectors in the Earth: Geophysics, **52**, 931-942.

Dong, W., 1999, AVO detectability against tuning and stretching artifacts: Geophysics, **64**, to appear in March.

Dong, W., and Keys, R.G., 1998, AVO inversion via localized migrations: SEG Expanded Abstracts, 178-181.